Machine Learning-Accelerated Method for Real-Time Optimization of Micro Energy-Water-Hydrogen Nexus

Mostafa Goodarzi and Qifeng Li, Senior Member IEEE

Abstract—This paper explores the micro Energy-Water-Hydrogen (m-EWH) nexus, an engineering system designed to reduce carbon emissions in the power sector. The m-EWH nexus leverages renewable energy sources (RES) to produce hydrogen via electrolysis, which is then combined with carbon captured from fossil fuel power plants to mitigate emissions. To address the uncertainty challenges posed by RES, this paper proposes a real-time decision-making framework for the m-EWH nexus, which requires the rapid solution of large-scale mixed-integer convex programming (MICP) problems. To this end, we develop a machine learning-accelerated solution method for real-time optimization (MARO), comprising three key modules: (1) an active constraint and integer variable prediction module that rapidly solves MICP problems using historical optimization data; (2) an optimal strategy selection module based on feasibility ranking to ensure solution feasibility; and (3) a feature space extension and refinement module to improve solution accuracy by generating new features and refining existing ones. The effectiveness of the MARO method is validated through two case studies of the m-EWH nexus, demonstrating its capability to swiftly and accurately solve MICP problems for this complex system.

Index Terms—Active constraints prediction, Energy water hydrogen nexus, Feature expansion, Feature refinement, Green hydrogen, Integer variables prediction, Machine learning, Mixed-integer convex program, Real-time optimization.

Nomenclature

A bbreviations

SSFR W2H

Abbrevia	ations
ACIVP	Active Constraints and Integer Variables Prediction
AEL	Alkaline Electrolysis
CCS	Carbon Capture Systems
EDWF	Electricity-Driven Water Facility
EWH	Energy-Water-Hydrogen
FC	Fuel Cell
FSER	Feature Space Extension and Refinement
HDN	Hydrogen Distribution Network
MARO	Machine Learning-Accelerated Solution Method for
	Real-Time Optimization
MICP	Mixed-Integer Convex Programming
m-EWH	Micro Energy-Water-Hydrogen
OMIO	Online Mixed-Integer Optimization
PDN	Power Distribution Network
PEM	Proton Exchange Membrane
RES	Renewable Energy Sources

WDN Water Distribution Network

This work is supported by U.S. National Science Foundation under Award

Wind-to-Hydrogen

Strategy Selection Based on Feasibility Ranking

CBET#2124849. (Corresponding Author: Qifeng Li)
The authors are with the Department of Electrical and Computer Engineering, University of Central Florida, Orlando, FL 32816 USA (e-mail: mostafa.goodarzi@ucf.edu, qifeng.li@ucf.edu).

Parameters

,	η .	Constant efficiency of the pump
l	$\xi_{ m e}^{ m dg}$	Carbon emission of a diesel generator factor
;	$\xi^{ m dsp}$	Hydrogen tank disappearance factor
	$\xi_{\rm p}^{\rm we}$	Energy for hydrogen production factor
•	ξ_{w}^{we}	Water for hydrogen production factor
•	ξfc	Hydrogen for power generation by FC factor
•	$\xi_{\mathrm{p}}^{\mathrm{we}}$ $\xi_{\mathrm{w}}^{\mathrm{we}}$ $\xi_{\mathrm{h}}^{\mathrm{fc}}$ ξ_{c}^{χ}	Chemical production by captured carbon factor
6	ρ^{χ}	Chemical production price
	A^{wt}	Water tank area
	d_n	Water demand at node n
	d^{we}	Water demand of water electrolysis
ì		Power for water production by desalination factors
l	$p^{\mathrm{l}},q^{\mathrm{l}}$	Active and reactive power load
t	p^{wind}	Wind power
,	$\stackrel{\scriptstyle P}{PR}$	Maximum reduced pressure value
•	r_q^{w}	Head loss coefficient of pipe q
l	-	Resistance and reactance of line ij
	r_{ij}, x_{ij}	Maximum apparent power of line ij
	$\frac{\overline{s}_{ij}}{\overline{s}^{hs}}$	Maximum apparent power of hydrogen system
ı	$v^{\mathrm{F}}, v^{\mathrm{R}}$	Forecasted and real wind speed
,	Variable	
	$b^{\mathrm{des}}, b^{\mathrm{p}}$	Binary variables related to desalination and pump
	$b^{ m fc}, b^{ m we}$	Binary variables related to FC and water electrolysis
	$c^{ m dg}$	Carbon emission of the diesel generator
	$c^{ m e}$	Emitted carbon to the atmosphere
	c^{s}, c^{χ} f^{des}	Captured carbon for storing and reusing
	•	Water production of desalination
	f_n, f_q f^{wt}	Water flow of node n and pipe q
	$h^{ m d}$	Water flow of water tank
	$h^{ m fc}$	Hydrogen demand of hydrogen loads
	h^{we}	Hydrogen demand of FC
		Hydrogen production by water electrolysis
	I^{χ}	Income from selling the chemical product
	\mathcal{I}_{ij}	Square of the current magnitude in line ij
	p_{ij}, q_{ij} p^{des}	Active and reactive power of line ij
		Power of water desalination
	$p^{ m dg}, q^{ m dg}$ $p^{ m fc}$	Active and reactive power of diesel generator
	$p^{\text{hs}}, q^{\text{hs}}$	FC output power
	p^{-},q^{-}	Active and reactive power of hydrogen system
		Power demand of pump
	$p^{\mathrm{sw}}, q^{\mathrm{sw}}$	Surplus active and reactive power of wind farm
	p^{t}	Transferred power to the power network
	$p^{ m we}$ $p^{ m wedg}$	Power of water electrolysis
	$p^{ m wedg}$ $V^{ m ht}$	Power of diesel generator for water electrolysis
l	$V^{ m nt}$ $V^{ m wt}$	Volume of hydrogen tank
_	V ***	Volume of water tank

Constant efficiency of the pump

Square voltage of bus i

Head gains imposed by the pump in the pipe q

Water head of the node n and the water tank

I. INTRODUCTION

THIS paper expands on the EWH nexus, initially introduced to mitigate carbon emissions on the power generation side of power systems [1], where fossil fuel power plants are equipped with CCS. Unlike conventional hydrogen production, the EWH nexus concentrates on green hydrogen from water electrolysis using RESs as an eco-friendly alternative. We introduce the m-EWH nexus, specifically designed for small communities like small islands, isolated coastal cities, and remote villages, where a single entity controls critical infrastructures. In these areas, which heavily rely on diesel generators with carbon emissions [2], [3], the m-EWH nexus emerges as a solution to curb carbon emissions, foster RESs integration, and address electrolysis' water intensity by proposing water network integration. Notably, our focus lies on the distribution side, highlighting the interconnections of water and power systems at this level, setting our study apart from previous works centered on the generation side.

Different RES, such as solar, wind, hydro, biomass, and geothermal, have been extensively studied in green hydrogen production [4]. This paper focuses on wind energy and W2H technology within the context of the m-EWH nexus. Notably, certain previous studies examining W2H applications did not consider wind uncertainty [5]-[8], relying instead on day-ahead wind speed predictions that may deviate from actual data [9]. Although several studies addressed wind energy uncertainty through probabilistic [10], robust optimization [11], and stochastic [12] methods, these optimization models under uncertainty have some significant limitations. For example, a deterministic approximation for a large engineering system is typically computationally intractable. In contrast, this paper proposes a real-time approach to optimize the operation of the m-EWH nexus, avoiding reliance on long-term wind forecasts exceeding 5 minutes. Instead of making decisions ahead-of-real-time, this paper proposes to solve the optimal operation of the m-EWH nexus in real-time, eliminating the reliance on long-term (longer than 5 minutes) wind forecasts. Despite the slow dynamics, hydrogen and water systems in the m-EWH nexus face significant uncertainty due to reliance on renewable energy, water scarcity, and variability in hydrogen demand, making it impractical to rely solely on large-scale storage.

This paper proposes a real-time decision-making scheme for hedging against uncertainty in the context of the *m*-EWH nexus. A convex mathematical model for *m*-EWH is employed to formulate the optimization problem as a real-time decision-making process, resulting in a large-scale MICP. Despite convexifying continuous non-convex constraints, the presence of binary variables in the optimization problem classifies it as MICP. Recently, there has been significant interest in using machine learning to address MICP. For example, in [13], they applied machine learning to fine-tune hyperparameters in optimization algorithms. Learning-based strategies have been explored to develop efficient branching rules for solving mixed-integer optimization problems [14]. A specialized method using

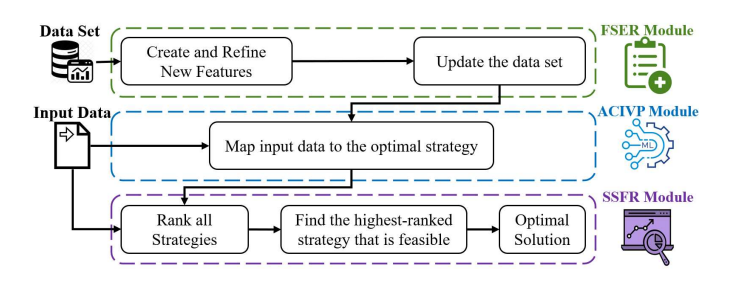


Fig. 1. Machine learning-accelerated for real-time optimization method.

neural networks has been proposed to solve MICP problems with logical constraints [15]. On the theoretical side, in [16], the authors analyzed the sample complexity involved in selecting cutting planes to use during the branch-and-cut algorithm of integer optimization solvers. Furthermore, in [17], the authors examined the sample complexity of learning high-quality hyperparameters in optimization algorithms. Despite these extensive efforts to solve MICP problems online, a gap remains between the solution times and the accuracy constraints required by many applications.

To address the computational challenges of solving this optimization problem in real-time with high accuracy, we introduce MARO which comprises three distinct modules: the ACIVP module, the SSFR module, and the FSER module (as shown in Fig. 1). Utilizing historical data, the ACIVP module maps input parameters to an optimal strategy to determine optimal values for binary variables and a set of active constraints [18]. The SSFR module ensures the feasibility of the proposed machine learning-accelerated approach. The FSER module enhances accuracy by developing new features derived from the raw data generated through offline optimization in the learning process. The FSER module includes two components: feature refinement and stage design and ordering. The feature refinement method evaluates predicted features at each stage and refines them as necessary. We delve into the impact of stage design and ordering on the performance of the FSER module, providing a comprehensive exploration of factors influencing its efficacy. These three modules work together to reduce the MICP problem to a smaller, continuous convex optimization problem that can be solved rapidly, enabling the application of MICP to online problems previously out of reach [19].

In summary, the main contribution and novelty of this paper lie in the development of the MARO approach, which can solve the MICP of the *m*-EWH nexus in real-time, ensuring both high accuracy and solution feasibility. The rest of this paper is organized as follows. Section II presents the system design and mathematical model of the *m*-EWH nexus. The optimization models for real-time operation are discussed in section III. Section IV explains the online solution method. Section V presents two case studies to validate this method. Finally, conclusions and future works are drawn in section VI.

II. MATHEMATICAL MODELS OF *m*-EWH NEXUS

This section explains the different components and the mathematical model of an *m*-EWH nexus. Fig. 2 shows a typical *m*-EWH nexus that includes a power section (red), a

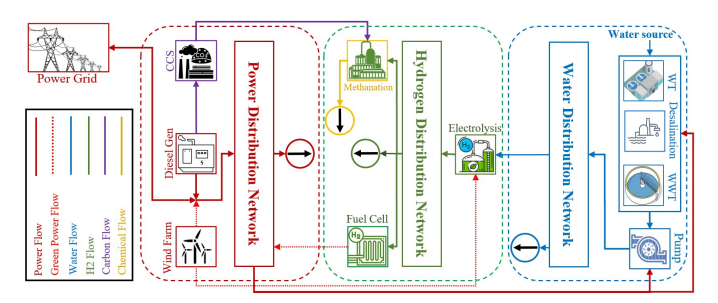


Fig. 2. A typical *m*-EWH nexus for remote coastal area: \rightarrow power, \rightarrow water, \rightarrow hydrogen, \rightarrow carbon, \rightarrow chemical product.

water section (blue), and a hydrogen section (green). This m-EWH nexus is designed for small communities in remote coastal cities/small islands, in which a unified entity controls the entire system. A diesel generator, enhanced with small-scale CCS [20], meets a significant portion of the PDN demand, while a wind farm provides green energy for electrolyzing water. Excess wind energy is fed into the PDN for flexible loads like EDWFs. When there is a surplus of wind energy, it can be transferred to the power grid, while during periods of heavier load, the power grid supports distribution-side loads. The water section includes the WDN and EDWFs. The hydrogen section includes electrolysis, HDN, methanation, and an FC unit. Hydrogen generated by electrolysis is used in various applications, including satisfying the hydrogen network's demand, methanation to reuse captured carbon, and converting unpredictable wind energy into controllable energy through FC units. In the following subsections, we explain the mathematical models of different components of the m-EWH nexus.

A. Power Section

Power flow in the PDN can be modeled using several formulations. The Distflow model involves bus variables and branch variables and can be used to model both active and reactive power flow in the PDN. The convex model of the power section is expressed by [21]:

$$V_{i,t} - V_{j,t} = 2(r_{ij}p_{ij,t} + x_{ij}q_{ij,t}) - (r_{ij}^2 + x_{ij}^2)\mathcal{I}_{ij,t},$$
 (1a)

$$p_{ij,t}^2 + q_{ij,t}^2 \le \mathcal{V}_{i,t} \mathcal{I}_{ij,t},\tag{1b}$$

$$\underline{\mathcal{V}}_{i}\overline{\mathcal{V}}_{i}\mathcal{I}_{ij,t} + \overline{s}_{ij}^{2}\mathcal{V}_{i,t} \leq \overline{s}_{ij}^{2}(\underline{\mathcal{V}}_{i} + \overline{\mathcal{V}}_{i})$$
 (1c)

$$p_{ij,t}^2 + q_{ij,t}^2 \le \bar{s}_{ij}^2, \tag{1d}$$

$$\sum_{k} (p_{ki,t}) + r_{ij} \mathcal{I}_{ij,t} - p_{ij,t} = p_{i,t}^{dg} + p_{i,t}^{sw} + p_{i,t}^{hs} - p_{i,t}^{l}, \quad (1e)$$

$$\sum_{t}^{n} (q_{ki,t}) + x_{ij} \mathcal{I}_{ij,t} - q_{ij,t} = q_{i,t}^{\text{dg}} + q_{i,t}^{\text{sw}} + q_{i,t}^{\text{hs}} - q_{i,t}^{l}, \quad (1f)$$

$$\underline{p}_{i}^{\mathrm{dg}}, \underline{q}_{i}^{\mathrm{dg}}, \underline{\mathcal{V}}_{i}, \underline{\mathcal{I}}_{ij} \leq p_{i,t}^{\mathrm{dg}}, q_{i,t}^{\mathrm{dg}}, \mathcal{V}_{i,t}, \mathcal{I}_{ij,t} \leq \overline{p}_{i}^{\mathrm{dg}}, \overline{q}_{i}^{\mathrm{dg}}, \overline{\mathcal{V}}_{i}, \overline{\mathcal{I}}_{ij}$$
(1g)

$$p_t^{\rm t} = p_t^{\rm wind} - (p_t^{\rm we} + p_t^{\rm sw}) + p_t^{\rm wedg}. \tag{1h} \label{eq:1h}$$

$$c_t^{\rm dg} = \xi_{\rm c}^{\rm dg} p_t^{\rm dg}, \tag{1i}$$

$$c_t^{\mathsf{e}} = c_t^{\mathsf{dg}} - c_t^{\mathsf{s}} - c_t^{\mathsf{\chi}},\tag{1j}$$

Constraints (1a) to (1d) are related to Ohm's law. The nodal balance of active and reactive power can be determined by (1e) and (1f), respectively. The upper and lower bounds for variables are described by (1g). The *m*-EWH nexus may not be able to capture all wind energy due to its volatility and

unpredictable characteristics. The power grid can serve as a large energy storage system for capturing excess wind power, as shown with (1h). Constraints (1i) and (1j) show the model of carbon emissions resulting from diesel generation, which consists of three parts: emitted parts, ones reused for chemical production, and ones stored [22].

B. Water Section

A convex-hull model for the water section of the *m*-EWH nexus, including water desalination, mass flow conservation law, pipe flow, water pumps, water tank, and pressure-reducing valves, is given [23]–[26]:

$$\widehat{Y} \begin{cases} \leq (2\sqrt{2} - 2)r_{q}^{w}\overline{f}_{q}f_{q,t} + (3 - 2\sqrt{2})r_{q}^{w}\overline{f}_{q}^{2}, \\ \geq (2\sqrt{2} - 2)r_{q}^{w}\underline{f}_{q}f_{q,t} - (3 - 2\sqrt{2})r_{q}^{w}\underline{f}_{q}^{2}, \\ \geq 2r_{q}^{w}\overline{f}_{q}f_{q,t} - r_{q}^{w}\overline{f}_{q}^{2}, \\ \leq 2r_{q}^{w}\underline{f}_{q}f_{q,t} + r_{q}^{w}\underline{f}_{q}^{2}. \end{cases}$$
(2a)

$$\sum_{m} f_{nm,t} = f_{n,t}^{\text{des}} - d_{n,t} + f_{n,t}^{\text{wt}}, \tag{2b}$$

$$p_t^{\text{des}} = e \times f_t^{\text{des}},\tag{2c}$$

$$e = \begin{cases} e_1, & 0 \le f_t^{\text{des}} \le 0.25 b_t^{\text{des}} \overline{f}^{\text{des}} \\ e_2, & 0.25 b_t^{\text{des}} \overline{f}^{\text{des}} \le f_t^{\text{des}} \le 0.5 b_t^{\text{des}} \overline{f}^{\text{des}} \\ e_3, & 0.5 b_t^{\text{des}} \overline{f}^{\text{des}} \le f_t^{\text{des}} \le 0.75 b_t^{\text{des}} \overline{f}^{\text{des}} \\ e_4, & 0.75 b_t^{\text{des}} \overline{f}^{\text{des}} \le f_t^{\text{des}} \le b_t^{\text{des}} \overline{f}^{\text{des}} \end{cases}$$

$$(2d)$$

$$\hat{Y} + y_{q,t}^{G} - r_q^{W}(f_{q,t})^2 \ge M(b_{q,t}^{P} - 1),$$
 (2e)

$$\widehat{Y} + y_{a,t}^{G} - r_a^{W} \overline{f}_a f_{q,t} \le M(1 - b_{a,t}^{P}), \tag{2f}$$

$$0 \le f_{q,t} \le b_{q,t}^{\mathbf{p}} \overline{f}_q, \tag{2g}$$

$$V_{n,t+1}^{\text{wt}} = V_{n,t}^{\text{wt}} + f_{n,t}^{\text{wt}},$$
 (2h)

$$A_n^{\text{wt}}(y_{n,t+1}^{\text{wt}} - y_{n,t}^{\text{wt}}) = f_{n,t}^{\text{wt}}, \tag{2i}$$

$$-PR \le \widehat{Y} \le PR,\tag{2j}$$

$$\eta p_{i,t}^{\mathbf{p}} \ge 2.725 \times (a_1(f_{q,t})^2 + a_0 f_{q,t}) \tag{2k}$$

$$\eta p_{i,t}^{\mathrm{p}} \le 2.725 \times (a_1 \overline{f}_q + a_0) f_{q,t},$$
 (21)

$$\underline{f}_{n}^{\text{des}}, \underline{f}_{n}^{\text{wt}}, \underline{V}_{n}^{\text{wt}} \leq f_{n,t}^{\text{des}}, f_{n,t}^{\text{wt}}, V_{n,t}^{\text{wt}} \leq \overline{f}_{n}^{\text{des}}, \overline{f}_{n}^{\text{wt}}, \overline{V}_{n}^{\text{wt}},$$
 (2m)

 $\underline{y}_{n}, \underline{f}_{p} \leq y_{n,t}, f_{p,t}, \leq \overline{y}_{n}, \overline{f}_{p}, \tag{2n}$

where $\widehat{Y} = y_{n,t} - y_{m,t} + h_q$, and h_q is the elevation difference between nodes n and m. Constraint (2a) shows a convex-hull model for head loss along a regular pipe. The equality of water injection and water output at each node is guaranteed by (2b). Equations (2c) and (2d) show a model of water desalination. The convex model of a pipe with a pump is expressed by (2e) to (2g). Each tank is modeled as a node using (2h) and (2i). Pressure-reducing valve is modeled by (2j) to control the water head pressure and the convex model of a pump is modeled by (2k) and (2l). The upper and lower levels of the variables are shown by (2m) and (2n). Please refer to [23]–[25] for more details on convex-hull formulation and accuracy.

C. Hydrogen Section

The following mathematical formulations describe the hydrogen section of the *m*-EWH nexus, which includes water electrolysis, an FC unit, a hydrogen tank, and a methanation

system:

$$h_t^{\text{we}} = \xi_p^{\text{we}} p_t^{\text{we}} \tag{3a}$$

$$d_t^{\text{we}} = \xi_{\text{w}}^{\text{we}} h_t^{\text{we}}, \tag{3b}$$

$$V_{t+1}^{\text{ht}} = (1 - \xi^{\text{dsp}})V_t^{\text{ht}} + (h_t^{\text{we}} - h_t^{\text{fc}} - h_t^{\text{d}}), \tag{3c}$$

$$p_t^{\text{fc}} = \xi_h^{\text{fc}} h_t^{\text{fc}}, \tag{3d}$$

$$(p_t^{\text{we}} - p_t^{\text{fc}})^2 + (q_t^{\text{hs}})^2 \le (\overline{s}^{\text{hs}})^2, \tag{3e}$$

$$b_t^{\text{fc}} \underline{h}^{\text{fc}}, b_t^{\text{we}} p^{\text{we}} \le h_t^{\text{fc}}, p_t^{\text{we}} \le b_t^{\text{fc}} \overline{h}^{\text{fc}}, b_t^{\text{we}} \overline{p}^{\text{we}}, \tag{3f}$$

$$\underline{V}^{\text{ht}} \le V_t^{\text{ht}} \le \overline{V}^{\text{ht}} \tag{3g}$$

$$I_t^{\chi} = \rho^{\chi} \, \xi_c^{\chi} \, c_t^{\chi}. \tag{3h}$$

$$b_t^{\text{we}} + b_t^{\text{fc}} \le 1, \tag{3i}$$

$$\sum_{l=0}^{T^s} \left(b_{t+l}^{\text{we}} \right) \begin{cases} = 0, & \text{if } b_t^{\text{we}} - b_{t-1}^{\text{we}} < 0\\ \ge 0, & \text{if } b_t^{\text{we}} - b_{t-1}^{\text{we}} \ge 0 \end{cases} , \qquad (3j)$$

where (3a) shows hydrogen production and (3b) represents the required water for the electrolysis process. A mass balance equation for H_2 is presented by (3c), which takes into account dissipation rates and the demand for H_2 in the HDN. Constraint (3d) refers to the H_2 consumption level of FC units based on efficiency and conversion factors, and (3e) presents the H_2 systems' inverter for reactive power support [27]. The upper and lower levels of water electrolysis power, hydrogen tank volume, and hydrogen rate of the FC unit are shown in (3f) and (3g). The simultaneous operation of electrolysis and FC units is avoided by (3i). The methanation system combines the captured carbon with hydrogen to generate CH_4 using a Sabatier reaction [28], we need 182 g of hydrogen to recycle 1 kg of carbon, which can be produced from 1.64 liters of water, based on the chemical equation for this process $(4H_2 + CO_2 \rightarrow CH_4 + 2H_2O)$. The income from selling chemical production is shown by (3h). As AEL is the most mature technology and has a lower installation cost than other water electrolysis technologies [29], we chose to incorporate this technology into the m-EWH nexus framework. Since AEL starting up takes approximately 30 to 50 minutes each [30], [31], we consider a 1-hour interval sufficient to change the ON/OFF status. The ON/OFF status of the AEL will be 0 for T^s continuous time intervals, totaling 1 hour, after the switch has been changed from ON to OFF, as indicated in (3j).

III. OPTIMIZATION MODELS FOR REAL-TIME OPERATION

The proposed m-EWH nexus requires actual wind speed to hatch against issues that occur by wind uncertainty in real-time optimal operation mode. This paper operates under the assumption that 5-minute-ahead wind predictions can be treated as real-time wind speeds, leading to the fixation of all binary variables in the following 5 minutes. Since the FC, desalination plant, and water pump can rapidly change their operational status [23], [32], controlling these devices is relatively straightforward. In contrast, AEL technology (which requires startup time and minimum working capacity) makes optimization more challenging. Optimization models for other water electrolysis technologies, such as solid oxide and PEM electrolysis, must be different. This section presents two optimization models for the real-time operation of the m-EWH nexus according to two different water electrolysis technologies. The objective function of these optimization models that minimizes carbon emissions and wind power transfer to the power grid, while maximizing revenue from the sale of chemical production is shown as:

$$\sum_{t=1}^{T} \left(a_1 p_t^{t} + a_2 p_t^{dg} + a_3 c_t^{e} + a_4 c_t^{s} - I_t^{\chi} \right), \tag{4}$$

where a_1 to a_4 are the parameters that show the penalty [33] or cost. The first and second terms of (4) aim to minimize power transfer to the power grid and power generation by the diesel generator, respectively. The third and fourth terms focus on reducing carbon emissions and stored carbon. The final term seeks to maximize income from selling the chemical product. Solution methods to achieve real-time optimal solutions at high speed are discussed in Section IV.

A. Optimization Model for Real-Time Decision-Making of m-EWH Nexus with AEL

AEL electrolysis is the most common water electrolysis technology and has a cost advantage in terms of installation, but it needs one hour for switching. Additionally, AEL electrolysis requires a minimum operating capacity of 20%. Due to the presence of devices such as water and hydrogen tanks that can store and utilize these resources throughout the day, an operation horizon of 24 hours should be considered in the optimization model of m-EWH nexus. Because of the time limitation associated with switching, we must determine the status of AEL for the next hour (the subsequent T^{s} time steps) at every time step. Here, T^{s} is set to 12, considering a switching time of 60 minutes and a time step of 5 minutes. The AEL status for the next hour is calculated and fixed for the next time step. Other binary variables can be changed in the following time step optimization. Algorithm 1 and Fig. 3 illustrate this model.

Algorithm 1: Optimal operation of *m*-EWH nexus with AEL

Input: day ahead forecasted of wind speed and power/water demand $\mathbb{W}_0 = \{v_1^{F_0},...,v_T^{F_0}\}, \ \mathbb{P}_0^L = \{p_1^{L,F_0},...,p_T^{L,F_0}\}, \ \text{and} \\ \mathbb{D}_0 = \{d_1^{F_0},...,d_T^{F_0}\}.$

1 Solve the mixed-integer problem to determine the optimal ON/OFF status for the initial hour of the day for AEL ($\mathbf{B}_{0}^{\mathbf{we}^{*}}$);

2 for i=1 to T do

Input real-time and day-ahead of wind speed and power/water

 $\begin{aligned} & \text{mod} & \text{demand:} \\ & \mathbb{W}_i = \{v_i^{F_i}, v_{i+1}^{F_i}, \dots, v_{i+T}^{F_i}\}, \ v_i^{F_i} = v_i^R, \\ & \mathbb{P}_i^{\mathsf{L}} = \{p_{i}^{\mathsf{LF}_i}, p_{i+1}^{\mathsf{LF}_i}, \dots, p_{i+T}^{\mathsf{LF}_i}\}, \ p_i^{\mathsf{LF}_i} = p_{i}^{\mathsf{LR}}, \\ & \mathbb{P}_i^{\mathsf{L}} = \{p_{i}^{\mathsf{LF}_i}, p_{i+1}^{\mathsf{LF}_i}, \dots, p_{i+T}^{\mathsf{LF}_i}\}, \ p_i^{\mathsf{LF}_i} = q_i^{\mathsf{LR}}, \end{aligned}$

 $\mathbb{D}_{i} = \{d_{i}^{F_{i}}, d_{i+1}^{F_{i}}, ..., d_{i+T}^{F_{i}}\}, d_{i}^{F_{i}} = d_{i}^{R};$

Fix the binary variables related AEL for T^{s} upcoming times to the values obtained in the previous optimization problem, $\mathbb{B}_i^{\mathrm{we}} = \mathbf{B}_{i-1}^{\mathrm{we}^*}$; Apply **Algorithm 2** mentioned in **subsection IV-A** to find the

surrogate optimization problem;

Solve the surrogate optimization problem;

Update the optimal values for the binary variables related to AEL for the next optimization problem;

11 end

The optimization model for the m-EWH nexus with AEL technology is shown as follows:



Fig. 3. Real-time optimization model for the *m*-EWH nexus with AEL technology: the intervals that filled with green color show the ON/OFF status of the AEL which should be fixed within the next $T^{\rm s}$ time intervals. The blue circles are obtained in the current optimization problem ($\mathbf{b}_{T^{\rm s}+1}^{\rm we*}$) and will be fixed in the following optimization problem (yellow circles).

$$\begin{aligned} & \text{min} \quad (4) \\ & s.t \quad (1) - (3) \\ & b_t^{\text{we}} = \mathbf{b}_t^{\text{we*}}, \quad \forall \ t \in \{1, ..., T^{\text{s}}\}, \\ & b_t^{\text{p}}, b_t^{\text{we}}, b_t^{\text{des}}, b_t^{\text{fc}} \in \{0, 1\}. \end{aligned}$$

B. Optimization Model for Real-time Decision-Making of m-EWH Nexus with PEM Technology

The *m*-EWH nexus may use other water electrolysis technologies, such as solid oxide and PEM electrolysis. Since solid oxide electrolysis is still in the research phase, our focus is on PEM technology, which has recently gained significant popularity [34]. PEM technology offers faster switching times and the ability to operate without a minimum load [29], [35]. As a result, we only need to solve the following optimization problem at each time step:

$$\begin{aligned} & \min & & (4) \\ & s.t & & (1) - (3), \\ & & b_t^{\mathrm{p}}, b_t^{\mathrm{we}}, b_t^{\mathrm{des}}, b_t^{\mathrm{fc}} \in \{0, 1\}. \end{aligned}$$

IV. MACHINE LEARNING-ACCELERATED SOLUTION METHOD

Since we propose to solve problems (5) and (6) in real-time, the computation efficiency of the solution method is critical. Even though we have convexified the non-convex constraints in these problems, the binary variables and the huge size still make the problem computationally challenging using conventional optimization methods. This section introduces the MARO approach, which is based on ACIVP, a new and fast solution method for solving MICP problems [19], to find the real-time optimal solution for the m-EWH nexus. The MARO method consists of three modules: the ACIVP module, the FSER module, and the SSFR module. These three modules replace (5) and (6) with a smaller-scale continuous convex optimization problem. The ACIVP module ensures rapid speed, the SSFR module ensures feasible solutions, and the FSER module enhances accuracy, ensuring highly precise results. Detailed explanations of these modules are provided in the following subsections.

A. ACIVP Module

We define active constraints as the set of constraints that are satisfied as equalities at optimality [36]. By identifying the active constraints, all other non-active constraints can be

removed since they do not influence the optimal solution. Therefore, predicting active constraints can reduce the size and complexity of a problem by removing redundant constraints, which reduces overall solution time. However, determining active constraints before solving an optimization problem is a challenge. The ACIVP module method tackles this by utilizing data-driven techniques to predict these This approach involves solving optimization problems, identifying relevant active constraints post-solution, and employing data-driven methods to predict future active constraints. Generally, the approach to generating this dataset largely depends on the specific practical application and available resources. Any solver or optimization method can be used to solve the related optimization problems. For example, using a distributed approach can increase the speed of creating the dataset. Notably, this predictive step occurs without solving the online optimization problem, and solving offline optimization problems does not notably impact the solution time of the online prediction process.

The same applies to determining optimal values for binary variables. The ACIVP method replaces the original problems with a new optimization problem by forecasting binary variables and active constraints using data-driven approaches, allowing us to apply MICP to real-time operations that were previously impractical. Fig. 4 illustrates this process for (6). Using the ACIVP module, the original problem with M constraints and binary variables is replaced by a surrogate problem with a smaller number of constraints (n), and the binary variables $(b_t^p, b_t^{\text{we}}, b_t^{\text{des}}, b_t^{\text{fc}})$ are replaced by their optimal values $(\mathbf{b}_{t}^{p^*}, \mathbf{b}_{t}^{tot}, \mathbf{b}_{t}^{des^*}, \mathbf{b}_{t}^{fc^*})$. Similarly, we have an equivalent process that applies to (5). So, we can update (2d) - (2g), and (3f) and replace binary variables by their optimal values. Now, the surrogate optimization problem is much easier than the original one because it has a smaller number of constraints and contains only continuous variables. We define the optimal strategy as a set of binary variables in the optimal values and active constraints. It is important to note that, despite solving optimization problems involving thousands of variables and constraints, the number of strategies remains limited to a few dozen or fewer [18]. ACIVP maps the input data, including real-time and forecasted values of wind speeds, water demand, and power demand, to the corresponding optimal strategy. Exploring the relationship between input and output data is achieved through machine learning techniques like decision trees, known for their effective classification performance.

$$\psi = \mathcal{H}(\varphi),\tag{7}$$

where φ and ψ are the input and output of the prediction

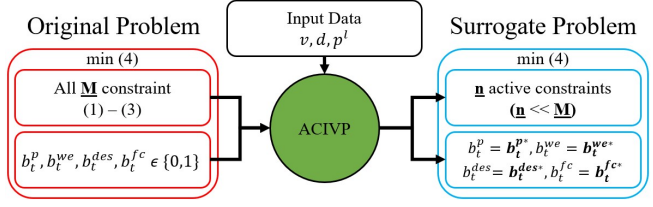


Fig. 4. Surrogate the original problem using the ACIVP module: input data are wind speed, water demand, and power demand.

model, respectively. The prediction model uses the dataset $\Gamma = \{(\varphi_1, \psi_1), (\varphi_2, \psi_2), ..., (\varphi_{\mathcal{N}_d}, \psi_{\mathcal{N}_d})\},$ which is created by solving offline optimization problems, for the training task. Creating a robust and accurate hypothesis function relies heavily on the quality of the training dataset, which is constructed by solving offline optimization problems. The process involves tackling \mathcal{N}_{d} independent optimization problems, leading to the generation of \mathcal{N}_{d} distinct samples that collectively form the training dataset. Particular attention must be given to crafting a high-quality dataset to ensure the resulting hypothesis function generalizes well to unseen data. The sampling process continues until there is a large enough set of distinct strategies. We use the missing strategies bound method and the Good-Turing estimator for the sampling procedure to build a training data set that covers all probable strategies [18], [37]. Once we have completed sampling and creating the dataset, we map its input data to its output data using the prediction function in (7). Algorithm 2 shows the ACIVP module for real-time optimal operation of the m-EWH nexus.

Algorithm 2: Solving the MICP of the *m*-EWH Using the ACIVP

Input: wind speed, water demand, and power loads

- Use (7) to find the optimal strategy including optimal values for binary variables and active constraints
 ψ = {b_t^{p*}, b_t^{ve*}, b_t^{des*}, b_t^{fe*}, γ^S};
- 2 Update (2d) (2g), and (3f) using optimal binary variables;
- 3 Remove the redundant constraints;
- 4 Develop a surrogate optimization problem;
- 5 Solve the surrogate optimization problem, which is smaller and continues, to obtain the optimal operation of m-EWH nexus;

Although the ACIVP module is promising and has been shown to solve some MICPs very quickly [18], it relies on its ability to identify optimal strategies accurately. Applying only the ACIVP module to solve the m-EWH nexus problem may be high risk since m-EWH is a large-scale, complex system [19]. Predicting active constraints and binary variables is much more challenging than predicting quantities that follow clear patterns, like power demands, since the relationship between inputs, including wind speed, water demand, and power demand, and outputs, such as active constraints and binary variables, is not yet well-established. The resulting optimal solutions can be discredited if the accuracy of the ACIVP module is not high enough, regardless of how fast they are generated. Therefore, the ACIVP module might not always make accurate predictions, potentially resulting in sub-optimal or infeasible solutions. It is particularly concerning for our real-time model, where any infeasibility or inaccuracy could cause problems. In the following subsections, we discuss the feasibility and accuracy issues of the ACIVP module and propose two modules to enhance them.

B. SSFR Module

The accuracy of the ACIVP module may be unsatisfactory for large-scale, complex problems [19] like (5) and (6). Therefore, the model may not always provide accurate predictions, leading to sub-optimal or infeasible solutions. To address this risk, [18] suggests selecting the *k*-most likely

classes instead of relying solely on the best-predicted class. The k-most likely classes method entails mapping input data to the k-most optimal strategies and then calculating the sub-optimality and infeasibility of these k strategies to determine the best one. However, determining appropriate value of k can be challenging. Additionally, in the optimal operation of the m-EWH nexus, we solve 288 optimization problems daily, with each problem solved every 5 minutes, and the optimal solution is consistently updated. Consequently, the optimal solution at each time slot has a minor impact on the overall optimal operation and can be adjusted in subsequent time steps. Thus, sub-optimality is not a significant issue for the optimal operation. Instead, improving feasibility probability is more critical. To address this, we introduce the SSFR module. This module employs a ranking approach where all strategies are classified and ranked based on their mappings in the classification section of the ACIVP module. Starting with the highest-ranked strategy, the SSFR evaluates the feasibility of each one until it finds the first feasible optimal strategy. As a result, this strategy is selected as the optimal strategy, ensuring feasible outcomes for the surrogate problem. Algorithm 3 shows how the SSFR identifies the best optimal strategy that ensures feasibility.

Algorithm 3: SSFR module to select the best feasible strategy

```
Input: wind speed, water demand, and power loads

1 for i = 1 to N_{\psi} do

2 | find \psi_i using (7) which is the i-most likely optimal strategy;

3 | if the surrogate problem using \psi_i is feasible then

4 | go to step 7;

5 | end

6 end

7 \psi_i is the best optimal strategy that is feasible;
```

C. FSER Module

The effectiveness of the ACIVP module crucially hinges on its ability to identify optimal strategies accurately. However, the ACIVP module may exhibit unsatisfactory accuracy when applied to large-scale problems. Although we have previously demonstrated the ability to reach a feasible optimal strategy, enhancing the accuracy of the ACIVP module remains a significant challenge. In response, we propose the FSER module to improve the accuracy of the ACIVP solution for addressing the complex optimal operation problem of the m-EWH nexus. Since the additional features can enhance learning performance [38], we propose to improve the accuracy of the ACIVP module by expanding the feature space. In the proposed FSER module, the input and output layers of each stage are designed with different learning targets, namely newly developed features, to correct mapping model learning errors. Through solving offline optimization problems, various types of raw data, such as optimal values of binary variables, are generated. An additional feature is introduced at each stage of the FSER module using raw data to improve learning accuracy. It depends on the learning targets to determine how many stages are needed in each case. Similar to (7), the prediction functions map the input data of each stage to the output data. These prediction functions for the FSER module are:

$$\begin{cases} \mathcal{F}_{1} = \mathcal{H}_{1}^{\text{FSER}}(\varphi), & \text{Stage 1} \\ \vdots & (8) \\ \psi = \mathcal{H}_{\mathcal{K}}^{\text{FSER}}(\{\varphi, \mathcal{F}_{1}, \mathcal{F}_{2}, \dots, \mathcal{F}_{\mathcal{K}-1}\}), & \text{Stage } \mathcal{K} \\ \text{re } \mathcal{F}_{1} \text{ is predicted as the first stage output. } \mathcal{F}_{1} \text{ is then} \end{cases}$$

where \mathcal{F}_1 is predicted as the first stage output. \mathcal{F}_1 is then added as an additional feature in stage two to enhance the accuracy of \mathcal{F}_2 , which is an output of the second stage. At the end of the final stage, all of the output data are predicted. Algorithm 4 and Fig. 5 show the FSER module for improving the prediction accuracy of the optimal strategy.

Algorithm 4: FSER module for improving the accuracy

```
Input: Input data: wind speed, water demand, and power loads 1 Define a new feature (\mathcal{F}_1) and predict it base on (8):  \mathcal{F}_1 = \mathcal{H}_1^{\text{FSER}}(\varphi);  2 for i=1 to \mathcal{K}-2 do 3 Develop new features using (8):  \mathcal{F}_{i+1} = \mathcal{H}_{i+1}^{\text{FSER}}(\varphi, \mathcal{F}_1, \dots, \mathcal{F}_i);  4 end 5 Predict the optimal strategy by using all of the developed features:  \psi = \mathcal{H}_{\kappa}^{\text{FSER}}(\{\varphi, \mathcal{F}_1, \mathcal{F}_2, \dots, \mathcal{F}_{\mathcal{K}-1}\});
```

While the ACIVP module uses (7) to predict the optimal values of all binary variables and the set of active constraints in one stage, the proposed FSER module includes $\mathcal K$ different stages and uses (8) to improve the accuracy of the prediction. In the first stage, the proposed method predicts a portion of binary variables in $\mathcal F_1$, which is used as an additional feature in the next stage. The input data of stage 2 will be updated with this value to improve its accuracy in the prediction of $\mathcal F_2$ which contains another portion of binary variables. The process will continue to the last stage, where all binary variables and active constraints will be predicted more accurately. After that, the related constraints will be updated and the surrogate problem will be developed. To conduct a successful analysis, it will be necessary to revise the initial dataset into $\mathcal K$ datasets using the following approach: Γ^{FSER}

$$\begin{cases} (\{\varphi_1\}, \{\mathcal{F}_{1,1}\}), \dots, (\{\varphi_{\mathcal{N}_d}\}, \{\mathcal{F}_{1,\mathcal{N}_d}\}) & \text{Stage 1} \\ (\{\varphi_1, \mathcal{F}_{1,1}\}, \{\mathcal{F}_{2,1}\}), \dots, (\{\varphi_{\mathcal{N}_d}, \mathcal{F}_{1,\mathcal{N}_d}\}, \{\mathcal{F}_{2,\mathcal{N}_d}\}), & \text{Stage 2} \end{cases}$$

$$\vdots$$

$$(\{\varphi_1, \dots, \mathcal{F}_{\mathcal{K}-1,1}\}, \{\mathcal{F}_{\mathcal{K},1}\}), \dots, (\{\varphi_{\mathcal{N}_d}, \dots, \mathcal{F}_{\mathcal{K}-1,\mathcal{N}_d}\}, \{\mathcal{F}_{\mathcal{K},\mathcal{N}_d}\}). & \text{Stage } \mathcal{K} \end{cases}$$

In the FSER module, the learning errors of the ACIVP module diminish gradually, leading to an increase in accuracy. However, achieving high accuracy in feature prediction at each stage can be challenging. To address this challenge, we propose a feature refinement method to enhance feature prediction, further improving the accuracy. Besides, The architecture of the FSER module, which focuses on incorporating more features and expanding the feature space to enhance learning accuracy, may have

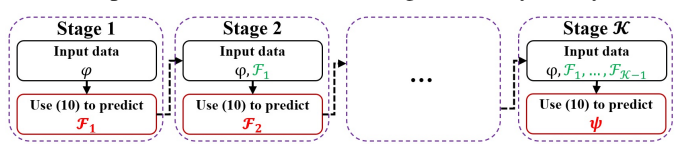


Fig. 5. FSER module for improving the prediction accuracy.

different stages and features depending on the application. We explain the feature refinement and stage design in the following subsection.

1) Enhancing Efficiency of FSER using Feature Refinement
The feature refinement method evaluates the predicted
features at each stage and refines them as necessary.
Algorithm 5 and Fig. 6 illustrate the iterative process of
feature refinement.

```
Algorithm 5: Feature development and refinement
```

```
Input: Input data

1 Define the first feature (\mathcal{F}_1) and predict it base on (8):

\mathcal{F}_1 = \mathcal{H}_1^{\text{FSER}}(\varphi);
2 Define the second feature (\mathcal{F}_2) and predict it base on (8):

\mathcal{F}_2 = \mathcal{H}_2^{\text{FSER}}(\varphi, \mathcal{F}_1);
3 while true do

4 | Develop the feature checker using \mathcal{F}'_1 = \mathcal{H}'_1^{\text{FSER}}(\varphi, \mathcal{F}_2);
5 | if |\mathcal{F}'_1 - \mathcal{F}_1| \leq \epsilon then
6 | break;
7 | end
8 | \mathcal{F}_1 \leftarrow \mathcal{F}'_1;
9 | go to line 2;
10 end
11 \mathcal{F}_1 and \mathcal{F}_2 are final developed refine features;
```

Initially, we generate \mathcal{F}_1 by mapping the original input data. Subsequently, we create \mathcal{F}_2 by mapping both the original input data and \mathcal{F}_1 . We then construct a feature checker (\mathcal{F}'_1) by mapping the original input data and \mathcal{F}_2 . It allows us to provide feedback to evaluate the accuracy of predicting \mathcal{F}_1 , refining it as necessary. If \mathcal{F}'_1 closely matches \mathcal{F}_1 , the two developed features are considered accurate. Otherwise, we replace \mathcal{F}_1 with \mathcal{F}'_1 and iterate this process until this criterion is met.

2) Stage Design and Ordering of FSER Module

This section proposes different methods for designing the FSER module to enhance the accuracy. Different scenarios are proposed to create new features, determine the number of stages, and develop the FSER module.

• Physical Features: New features can be created through consideration of the physical interpretation of the problem. The suggested design is beneficial for solving problems that involve various types of equipment with binary variables in their models. We begin by predicting binary variables related to a specific piece of equipment. This prediction is then used as a feature to enhance the accuracy of predicting another set of binary variables associated with other types of equipment. This procedure continues until the final stage. For example, the mathematical model of the m-EWH nexus contains binary variables for four equipment types: pumps, desalination, FC, and electrolysis. Therefore, we can divide the binary variables into four groups based on their physical meaning, and each group of these four groups is assigned to a specific stage. The features are

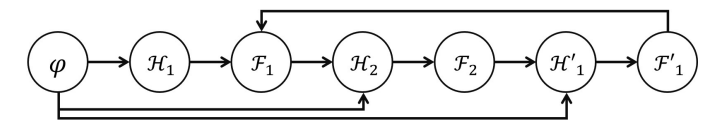


Fig. 6. Feature development and refinement.

TABLE I FEATURE SELECTION METHODS AND CORRESPONDING FEATURES

${\bf Method} \qquad N_{\bf Stage}$		Features		
Physical	5	$oldsymbol{b_t^{p^*}}, oldsymbol{b_t^{des^*}}, oldsymbol{b_t^{fe^*}}, oldsymbol{b_t^{we^*}}, oldsymbol{\gamma^{S}}$		
Time	289	$\mathbf{b}_{k}^{\mathbf{p^*}}, \mathbf{b}_{k}^{\mathbf{des^*}}, \mathbf{b}_{k}^{\mathbf{fe^*}}, \mathbf{b}_{k}^{\mathbf{we^*}}, \gamma^{\mathrm{S}}, \forall \ k \in \{1,, 288\}$		
Number	2017	$\mathbf{b_{4k-3}^{p^*}, b_{4k-2}^{des^*}, b_{4k-1}^{fe^*}, b_{4k}^{we^*}, \gamma^{\text{S}}, \forall \ k \in \{1,, 288\}}$		
Coupled	3	$\{\mathbf{b^{p^*}}, \mathbf{b^{des^*}}\}, \{\mathbf{b^{fe^*}}, \mathbf{b^{we^*}}\}, \gamma^{S}$		

 $\{\mathcal{F}_1, \mathcal{F}_2, \mathcal{F}_3, \mathcal{F}_4, \mathcal{F}_5\} = \{\mathbf{b}_t^{\mathbf{p}^*}, \mathbf{b}_t^{\mathbf{des}^*}, \mathbf{b}_t^{\mathbf{fc}^*}, \mathbf{b}_t^{\mathbf{we}^*}, \gamma_t^S\}$. We develop a five-stage FSER module for our optimization model, which improves the accuracy.

- Temporal Features: Another approach to dividing binary variables and active constraints is based on temporal features. A dataset consisting of \mathcal{T} time steps is examined, and binary variables are divided into \mathcal{T} distinct groups, thereby generating \mathcal{T} novel features. This design can be suitable for solving problems that involve multi-periodic operations. The binary variables associated with the first time step will be predicted and used as supplementary features in the second stage. This process will persist until the final stage. For example, the m-EWH nexus model has four types of binary variables over \mathcal{T} time steps. We can group the binary variables into \mathcal{T} groups based on time and assign each group to a specific stage. So, the set of new features is $\mathcal{F}_k = \{\mathbf{b}_k^{\mathbf{p}^*}, \mathbf{b}_k^{\mathbf{des}^*}, \mathbf{b}_k^{\mathbf{fe}^*}, \mathbf{b}_k^{\mathbf{we}^*}, \gamma_k^{\mathbf{S}}\}, \forall k \in \{1, 2, ..., \mathcal{T}\}.$
- Number of Binary Variables Features: Another method for categorizing binary variables involves dividing them based on their quantity. Our proposal suggests dividing the binary variables into \mathcal{K} groups, where each group has an equal number of binary variables, regardless of their physical interpretation. This process results in \mathcal{K} separate stages within the dataset, each containing \mathcal{K} distinct features. Since this design is based on the number of facilities with binary variables in their models, it will differ for different m-EWH nexus case studies.
- **Correlation Features:** We propose to predict a certain binary variable and use it as a new feature for the prediction of another binary variable that shares some high degree of interdependence. The new features could provide a more comprehensive understanding of the underlying relationships and improve accuracy and performance. For example, (3i) indicates a strong relationship between binary variables of FC units and electrolysis in a *m*-EWH nexus operation. Predicting one variable early and using it as an additional feature for predicting the other can improve accuracy.

Table I summarizes the stage design method and provides a clear overview of all selected features, including the number of stages (ranging from 3 to 2017 stages) and justifications for their inclusion based on relevant parameters.

V. CASE STUDY

A. Introducing Test Beds

We demonstrate the robustness of the proposed method by examining it on two test beds as shown in Fig. 7 and Fig. 8.

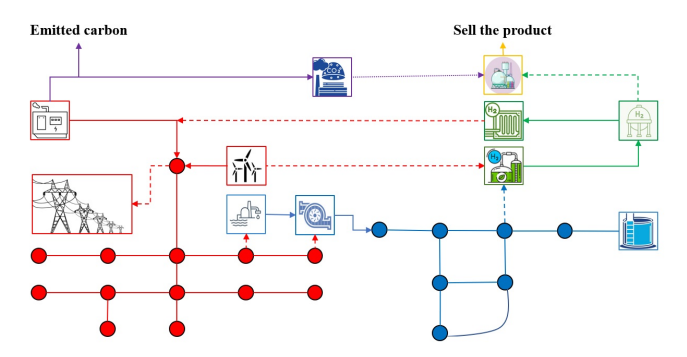


Fig. 7. A m-EWH nexus for a small stand-alone coastal city

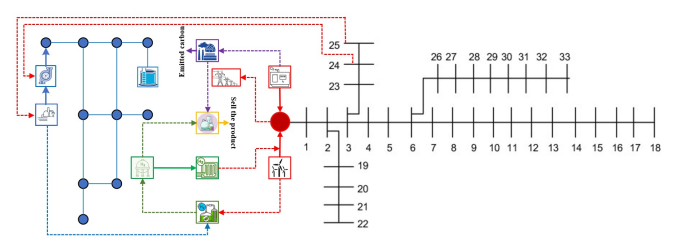


Fig. 8. A m-EWH nexus for a small stand-alone island

The IEEE 13-bus system with an 8-node EPANET WDN can represent a small stand-alone coastal city and the 33-bus distribution system with a 13-node Otsfeld WDN can be used for a remote small island. The first case study has 41474 constraints and 107717 variables, while the second has 82947 constraints and 246536 variables. Power, water, and hydrogen systems are distinct entities on a larger scale, and they have conflicts between them, making their collaboration impractical. Training data sets are built by solving offline optimization problems using wind speed and load data. 24-hour wind speed curves are extracted between 2008 and 2022 [39] and interpolated using spline interpolation every five minutes. 24-hour nodal load curves of power demand, excluding water pumps and desalination, are also extracted [40] and interpolated every five minutes. The same data collection can be used for practical systems until the m-EWH nexus concept is widely adopted. Once the m-EWH nexus becomes more common, real operational data from existing m-EWH systems can be collected and used. Upon dataset construction, we evaluate the proposed methods using real data, including actual wind speed and load data, derived from the Midcontinent Independent System Operator [41]. For each case study, we utilize these data to determine the optimal operation of the m-EWH nexus, incorporating two distinct water electrolysis technologies. The optimal operations are obtained by solving the related optimization problems using the MOSEK solver through Yalmip. All simulations are performed in the MATLAB R2019b environment on a system with an Intel Core i7-9700 CPU running at 3 GHz and 16 GB of RAM.

B. Importance of Online Optimization for m-EWH Nexus We employ real-time optimization models from section III to

achieve optimal operation of the proposed *m*-EWH nexus. Fig. 9 illustrates the optimal operation for the initial three consecutive time intervals. The black line denotes the power load demand, encompassing the water pump, desalination,

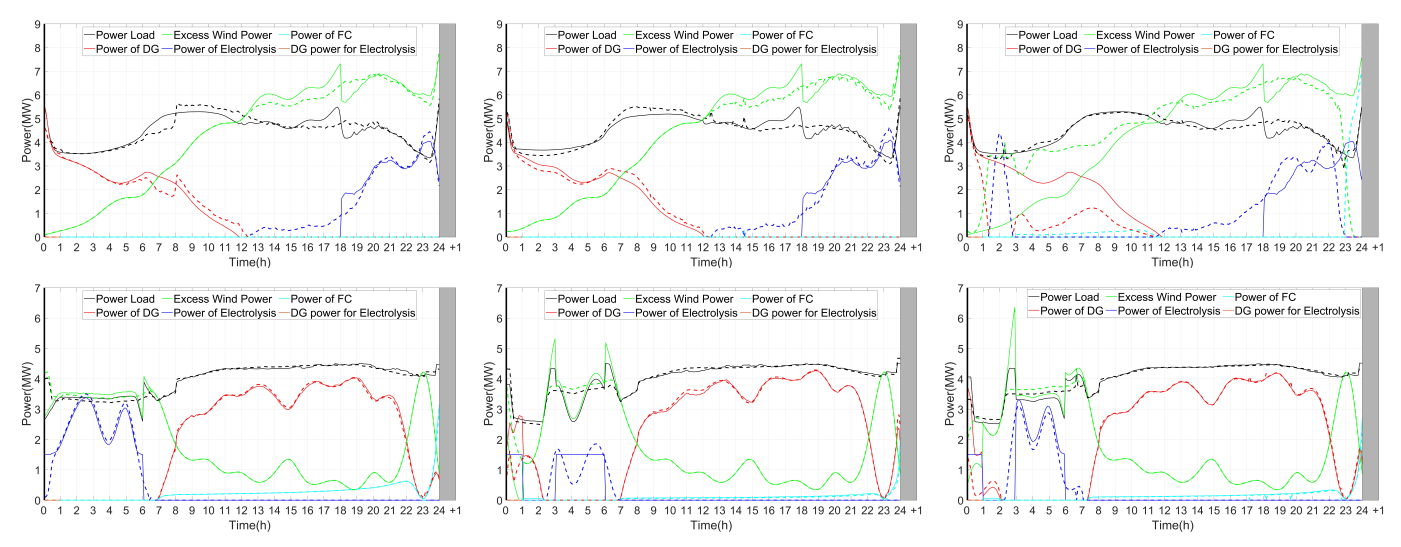


Fig. 9. *m*-EWH nexus optimal operation in three consecutive time steps (00:05, 00:10, 00:15). First row: the first case study (AEL: solid line. PEM: dashed line), second row: the second case study (AEL: solid line. PEM: dashed line).

and PDN loads. Red represents diesel power generation, green shows available wind energy after water electrolysis, blue indicates power demand for electrolysis, cyan represents FC unit power, and orange depicts diesel generator power for AEL electrolysis when wind energy is low. In this figure, the dashed line corresponds to the m-EWH nexus with PEM water electrolysis, while the solid line corresponds to the m-EWH nexus with AEL water electrolysis. This figure underscores the critical need for real-time optimal operation of the m-EWH nexus, as any deviation between forecasted and actual wind speeds can significantly impact optimal operation. Therefore, it is imperative to solve the related optimization problem rapidly to adjust the system's operation for optimal performance. By implementing the real-time optimal operation of the proposed m-EWH nexus, we can significantly reduce costs while achieving a better balance between supply and demand, leading to more efficient resource management. This system enhances sustainability by capturing and reusing all carbon emissions, contributing to a more resilient and environmentally friendly energy infrastructure. Additionally, it maximizes wind energy harvesting without compromising grid stability. The m-EWH nexus effectively addresses capacity limitations that often lead to renewable energy curtailments, ensuring the smooth and reliable integration of wind energy into the grid. These advancements result in a more sustainable, cost-effective, and robust energy system.

C. Evaluating the Solution Time of the MARO Method

Solving the *m*-EWH nexus optimization problems through conventional approaches is a lengthy process that requires over 15 minutes. Employing the proposed methods, we can replace the initial problem with a surrogate one, and achieve optimal real-time operation of the *m*-EWH nexus in just a few seconds. Table II compares the solution times of conventional approaches, the OMIO method [19], and the proposed MARO method for two case studies. The conventional approach involves solving the MICP directly using established optimization solvers. In contrast, OMIO, a

leading academic solution method, enhances solution speed by leveraging machine learning techniques. It learns the mapping between key problem parameters and an encoded optimal solution for integer variables and active constraints. On the other hand, the MARO method comprises three modules designed to accelerate solution times, ensure a feasible solution, and maintain high result accuracy. Table II illustrates the superior efficacy of the OMIO and MARO methods. The current assumption is that a 5-minute ahead wind speed prediction is sufficiently accurate, and simulations are conducted based on this assumption. According to Table II, if we have access to wind speed predictions with a lead time of 1 minute or less, the MARO method demonstrates the capability to achieve optimal operation of the m-EWH nexus. This is possible because the required solution time for this method is only a few seconds. The solution times of the OMIO and MARO methods are similar after finding the surrogate problem. Both methods can solve the optimization problem in seconds. However, the key difference lies in the accuracy of finding optimal values for binary variables and active constraints, where the MARO method enhances the feasibility and accuracy. In the following subsection, we will compare and discuss these differences.

TABLE II SOLUTION TIME OF OPTIMIZATION METHODS

Casa Study		Time	Solution Time (s)			
Case S	Case Study		Conventional	OMIO	MARO	
	AEL	00:05	936.41	1.62	1.63	
		00:10	892.16	1.82	1.47	
First		00:15	914.53	1.32	1.83	
THSt	PEM	00:05	592.70	1.24	1.07	
		00:10	562.99	1.31	1.19	
		00:15	984.50	1.15	1.38	
	AEL	00:05	1294.41	2.89	3.03	
		00:10	1263.74	4.09	3.67	
Second		00:15	1986.70	2.96	3.11	
Second	PEM	00:05	873.07	3.03	2.86	
		00:10	873.20	2.69	2.86	
		00:15	1011.04	3.17	2.98	

TABLE III
FEASIBILITY ASSESSMENT OF OMIO AND MARO METHODS

Case	OMIO	(k-most op	timal) (%)	MARO (SSFR module) (%)	
Case	k = 1	k = 10	k = 20	WARO (331 K module) (70)	
I	73	90	95	100	
II	69	91	94	100	

Case	OMIO (%)	MARO (%)			
		Physical	Time	Number	Coupled
I	77.58	98.92	94.53	88.72	94.17
II	74.91	97.73	93.17	87.32	93.46

D. Feasibility and Accuracy Evaluation

This section evaluates the potential shortcomings of the ACIVP module, which may occasionally result in inaccurate predictions and suboptimal or infeasible solutions. Table III compares the feasibility percentages of the OMIO method, which relies only on ACIVP, and the proposed MARO method. This table demonstrates that the k-most optimal strategy in OMIO method increases feasibility from 73% (for k = 1 which is the only ACIVP module) to 90% (for k = 10) and 95% (for k = 20) in the first case study, and from 69% to 91% and 94% in the second case study. Ultimately, the SSFR module in the proposed MARO method achieves a feasibility rate of 100%, demonstrating its effectiveness in improving the feasibility of the proposed method.

After refining the feasibility, we introduced the FSER module as a means to enhance the accuracy. This strategy includes developing new features with iterative refinement through multiple stages, to increase overall accuracy. The first design is a physical features-based design, resulting in a five-stage MARO with stages related to the pump, water desalination, FC units, water electrolysis, and active constraints. The second design is based on time, dividing binary variables into 288 time intervals of 24 hours. This results in a 289-stage MARO with 288 stages related to binary variables and one stage related to active constraints. The third design is based on the number of binary variables. Binary variables are divided into two groups to create a three-stage MARO. The last one is based on correlation, combining FC units and water electrolysis into one group and water pumps and desalination into another, resulting in a three-stage MARO with two stages related to binary variables and one stage related to active constraints. Table IV displays the accuracy of each design. This table shows that the proposed MARO method increases the accuracy. Out of four suggested design types, the physical design shows the greatest level of precision with a score of 98.92%.

VI. CONCLUSION AND FUTURE WORK

This paper introduces a machine learning-accelerated method for real-time optimization of the *m*-EWH nexus, aiming to reduce carbon emissions while maximizing wind energy utilization. By utilizing wind energy, hydrogen can be produced through electrolysis along with captured carbon to mitigate power sector carbon emissions. The paper develops

MICP models and control strategies based on water electrolysis technology to achieve optimal operation. To address the computational challenges involved in solving MICP, the paper introduces the MARO method, which comprises three modules. The ACIVP module predicts binary variable values and a limited set of constraints likely to contain all active constraints based on historical optimization data. Furthermore, the MARO method enhances feasibility and accuracy by implementing the SSFR and FSER modules. The SSFR module ensures the feasibility of the solution, increasing the feasibility probability to around 70%. The FSER module incorporates a multi-stage design with iterative refinement to develop new features, resulting in a 27.44% improvement in accuracy. Two case studies of the m-EWH nexus validate the proposed system and solution method, demonstrating significant reductions in solution time and improvements in accuracy and feasibility. This enables real-time optimal operation of the m-EWH nexus, effectively addressing the intermittent nature of wind energy and power demand.

In future work, we aim to explore contingencies in power, water, and hydrogen systems to ensure secure and resilient operations. We will evaluate the application of the MORA method in security-constrained optimization problems, focusing on identifying critical contingencies and solving these problems efficiently. To further enhance system intelligence and reduce computational costs, we plan to explore and compare machine learning classification methods for accurately predicting active constraints and binary variables. Additionally, we will explore hybrid optimization methods that combine metaheuristics with traditional techniques to improve solution robustness. Finally, we intend to collaborate with public administration experts to address potential regulatory challenges.

REFERENCES

- [1] M. Goodarzi and Q. Li, "Economic viability of the energy-water-hydrogen nexus for power system decarbonization," *arXiv preprint arXiv:2311.11111*, 2023.
- [2] M. Yousefzadeh, M. Lenzen, E. K. Tyedmers, and S. H. Ali, "An integrated combined power and cooling strategy for small islands," *Journal of Cleaner Production*, vol. 276, p. 122840, 2020.
- [3] P. Wijayatunga, L. George, A. Lopez, and J. A. Aguado, "Integrating clean energy in small island power systems: Maldives experience," *Energy Procedia*, vol. 103, pp. 274–279, 2016.
- [4] M. Goodarzi and Q. Li, "Exploring green hydrogen applications and optimization methods in the power sector: A comprehensive review," Jan. 2024. [Online]. Available: http://dx.doi.org/10.36227/ techrxiv.170491490.08174705/v1
- [5] F. Wei, Q. Sui, X. Li, X. Lin, and Z. Li, "Optimal dispatching of power grid integrating wind-hydrogen systems," *International Journal* of Electrical Power & Energy Systems, vol. 125, p. 106489, 2021.
- [6] L. He, Z. Lu, J. Zhang, L. Geng, H. Zhao, and X. Li, "Low-carbon economic dispatch for electricity and natural gas systems considering carbon capture systems and power-to-gas," *Applied energy*, 2018.
- [7] X. Zhang and Y. Zhang, "Environment-friendly and economical scheduling optimization for integrated energy system considering powerto-gas technology and carbon capture power plant," *Journal of Cleaner Production*, vol. 276, p. 123348, 2020.
- [8] K. Sun, K.-J. Li, Z. Zhang, Y. Liang, Z. Liu, and W.-J. Lee, "An integration scheme of renewable energies, hydrogen plant, and logistics center in the suburban power grid," *IEEE Transactions on Industry Applications*, vol. 58, no. 2, pp. 2771–2779, 2021.

- [9] R. Khezri, A. Mahmoudi, and M. H. Haque, "A demand side management approach for optimal sizing of standalone renewablebattery systems," IEEE Transactions on Sustainable Energy, vol. 12, no. 4, pp. 2184–2194, 2021.
- [10] Y. Li, B. Wang, Z. Yang, J. Li, and G. Li, "Optimal scheduling of integrated demand response-enabled community-integrated energy systems in uncertain environments," IEEE Transactions on Industry Applications, vol. 58, no. 2, pp. 2640-2651, 2021.
- [11] C. Gu, C. Tang, Y. Xiang, and D. Xie, "Power-to-gas management using robust optimisation in integrated energy systems," Applied energy, vol. 236, pp. 681–689, 2019.
- [12] X. Wu, H. Li, X. Wang, and W. Zhao, "Cooperative operation for wind turbines and hydrogen fueling stations with on-site hydrogen production," IEEE Transactions on Sustainable Energy, vol. 11, no. 4, pp. 2775–2789, 2020.
- [13] M.-F. Balcan, T. Sandholm, and E. Vitercik, "Learning to optimize computational resources: Frugal training with generalization guarantees," in Proceedings of the AAAI Conference on Artificial Intelligence, vol. 34, no. 04, 2020, pp. 3227-3234.
- [14] A. M. Alvarez, Q. Louveaux, and L. Wehenkel, "A machine learningbased approximation of strong branching," INFORMS Journal on Computing, vol. 29, no. 1, pp. 185-195, 2017.
- [15] A. Cauligi, P. Culbertson, E. Schmerling, M. Schwager, B. Stellato, and M. Pavone, "Coco: Online mixed-integer control via supervised learning," IEEE Robotics and Automation Letters, vol. 7, no. 2, pp. 1447-1454, 2021.
- [16] M.-F. F. Balcan, S. Prasad, T. Sandholm, and E. Vitercik, "Structural analysis of branch-and-cut and the learnability of gomory mixed integer cuts," Advances in Neural Information Processing Systems, vol. 35, pp. 33 890-33 903, 2022
- [17] M.-F. Balcan, D. DeBlasio, T. Dick, C. Kingsford, T. Sandholm, and E. Vitercik, "How much data is sufficient to learn high-performing algorithms? generalization guarantees for data-driven algorithm design," in Proceedings of the 53rd Annual ACM SIGACT Symposium on Theory of Computing, 2021, pp. 919-932.
- [18] D. Bertsimas and B. Stelato, "The voice of optimization," Machine Learning, vol. 110, no. 2, pp. 249-277, 2021.
- [19] D. Bertsimas and B. Stellato, "Online mixed-integer optimization in milliseconds," INFORMS Journal on Computing, 2022.
- Technip Energies. (2024) Carbon capture, utilization, and storage (ccus) - ten corporation, Accessed: Jan 2024, [Online], Available: https://www.ten.com/en/carbon-capture-utilization-and-storage-ccus
- [21] Q. Li and V. Vittal, "Convex hull of the quadratic branch ac power flow equations and its application in radial distribution networks," IEEE Transactions on Power Systems, vol. 33, no. 1, pp. 839-850, 2017.
- [22] A. Akbari-Dibavar, B. Mohammadi-Ivatloo, K. Zare, T. Khalili, and A. Bidram, "Economic-emission dispatch problem in power systems with carbon capture power plants," IEEE Transactions on Industry Applications, vol. 57, no. 4, pp. 3341–3351, 2021.
 [23] M. Goodarzi and Q. Li, "Evaluate the capacity of electricity-driven
- water facilities in small communities as virtual energy storage," Applied Energy, vol. 309, p. 118349, 2022.
- [24] Q. Li, S. Yu, A. S. Al-Sumaiti, and K. Turitsyn, "Micro waterenergy nexus: Optimal demand-side management and quasi-convex hull relaxation," IEEE Trans. Control. Netw. Syst., vol. 6, no. 4, pp. 1313-1322, 2018,
- [25] M. Goodarzi and Q. Li, "Hybrid physics and data-driven contingency filtering for security operation of micro energy-water nexus," CSEE Journal of Power and Energy Systems, 2023.
- [26] Q. Li, S. Yu, A. Al-Sumaiti, and K. Turitsyn, "Modeling and cooptimization of a micro water-energy nexus for smart communities," in 2018 IEEE PES Innovative Smart Grid Technologies Conference Europe (ISGT-Europe). IEEE, 2018, pp. 1-5.
- [27] H. Haggi, W. Sun, J. M. Fenton, and P. Brooker, "Proactive rollinghorizon-based scheduling of hydrogen systems for resilient power grids," IEEE Transactions on Industry Applications, vol. 58, no. 2, pp. 1737-1746, 2022
- [28] Y. Li, W. Liu, M. Shahidehpour, F. Wen, K. Wang, and Y. Huang, "Optimal operation strategy for integrated natural gas generating unit and power-to-gas conversion facilities," IEEE Transactions on Sustainable Energy, vol. 9, no. 4, pp. 1870-1879, 2018.
- [29] M. Scolaro and N. Kittner, "Optimizing hybrid offshore wind farms for cost-competitive hydrogen production in germany," International Journal of Hydrogen Energy, vol. 47, no. 10, pp. 6478-6493, 2022.
- [30] M. Götz, J. Lefebvre, F. Mörs, A. M. Koch, F. Graf, S. Bajohr, R. Reimert, and T. Kolb, "Renewable power-to-gas: A technological and economic review," Renewable energy, vol. 85, pp. 1371-1390, 2016.

- [31] J. Chi and H. Yu, "Water electrolysis based on renewable energy for hydrogen production," Chinese Journal of Catalysis, vol. 39, no. 3, pp. 390-394, 2018.
- [32] W. Daud, R. Rosli, E. Majlan, S. Hamid, R. Mohamed, and T. Husaini, "Pem fuel cell system control: A review," Renewable Energy, vol. 113, pp. 620-638, 2017.
- C. Shao, Y. Ding, and J. Wang, "A low-carbon economic dispatch model incorporated with consumption-side emission penalty scheme," Applied Energy, vol. 238, pp. 1084-1092, 2019.
- [34] A. Bahrami, F. Soltanifar, P. Fallahi, S. S. Meschi, and A. Sohani, "Energy and economic advantages of using solar stills for renewable energy-based multi-generation of power and hydrogen for residential buildings," *Buildings*, vol. 14, no. 4, p. 1041, 2024. H. J. Undertaking, "Study on early business cases for h2 in energy
- storage and more broadly power to h2 applications," 2017.
- [36] H. Bernau, "Active constraint strategies in optimization," in Geophysical Data Inversion Methods and Applications: Proceedings of the 7th International Mathematical Geophysics Seminar held at the Free University of Berlin, February 8-11, 1989. Springer, 1990, pp. 15-
- [37] I. J. Good, "The population frequencies of species and the estimation of population parameters," Biometrika, vol. 40, no. 3-4, pp. 237-264, 1953.
- [38] B. Liu, R. Tang, Y. Chen, J. Yu, H. Guo, and Y. Zhang, "Feature generation by convolutional neural network for click-through rate prediction," in The World Wide Web Conference, 2019, pp. 1119-1129.
- Meteoblue, "Hourly wind speed." [Online]. Available: https://www. meteoblue.com/en/weather/archive/export
- [Online]. Available: https://dataminer2.pjm.com/feed/hrl_load_metered
- [41] MISO, "Real-time and market data." [Online]. Available: https: //api.misoenergy.org/MISORTWD/operations.html?realTimeTotalLoad



Mostafa Goodarzi received the B.S. and M.S. degrees in Electrical Engineering from Amirkabir University of Technology, Tehran, Iran, in 2010 and 2012, respectively. His previous job experience included working as a Research Engineer and Project Manager at Niroo Research Institute, Tehran, Iran, from 2012 to 2019. Currently, he is working as a Graduate Research and Teaching Assistant for the Department of Electrical and Computer Engineering, University

of Central Florida, Orlando, FL, USA. His research interests include ML-based optimization methods, optimal operation, demand response, and integrated systems.



Qifeng Li (S'14, M'16, SM'20) received the Ph.D. degree in electrical engineering from Arizona State University, Tempe, AZ, USA, in 2016. He is currently an Assistant Professor with the Department of Electrical and Computer Engineering, University of Central Florida (UCF), Orlando, FL, USA. Before joining UCF, he held a position of Postdoctoral Associate with the Department of Mechanical Engineering,

Massachusetts Institute of Technology, Cambridge, MA, USA, from 2016 to 2018. His research interests include deterministic or uncertain optimization and nonlinear systems with applications in power and energy systems.